NANO LETTERS

Letter

pubs.acs.org/NanoLett

Terms of Use CC-BY

Photovoltaic Effect in an Electrically Tunable van der Waals Heterojunction

Marco M. Furchi,[†] Andreas Pospischil,[†] Florian Libisch,[‡] Joachim Burgdörfer,[‡] and Thomas Mueller*,[†]

[†]Institute of Photonics, Vienna University of Technology, Gußhausstraße 27-29, 1040 Vienna, Austria

[‡]Institute for Theoretical Physics, Vienna University of Technology, Wiedner Hauptstraße 8-10, 1040 Vienna, Austria

Supporting Information

ABSTRACT: Semiconductor heterostructures form the cornerstone of many electronic and optoelectronic devices and are traditionally fabricated using epitaxial growth techniques. More recently, heterostructures have also been obtained by vertical stacking of two-dimensional crystals, such as graphene and related two-dimensional materials. These layered designer materials are held together by van der Waals forces and contain atomically sharp interfaces. Here, we report on a type-II van der Waals heterojunction made of molybdenum disulfide and tungsten diselenide monolayers. The junction is electrically tunable, and under appropriate gate bias an atomically thin diode is realized. Upon optical illumination, charge transfer occurs across the planar interface and the device exhibits a photovoltaic effect. Advances in large-scale production of two-dimensional crystals could thus lead to a new photovoltaic solar technology.

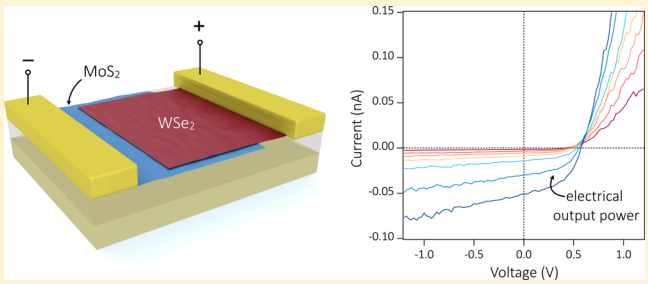

KEYWORDS: *2D materials, transition-metal dichalcogenides, van der Waals heterostructures, photovoltaics*

The discovery of the photovoltaic effect in a silicon p−n junction by Chapin, Fuller, and Pearson[1] heralded the era of photovoltaics. Although today's technology is still mainly based on silicon, a multitude of other materials have been investigated since then, with perovskite[2] being one of the most recent additions. Lately, a new class of materials has emerged, two-dimensional (2D) atomic crystals.[3,4] These can be produced with large area dimensions at low costs and on flexible substrates,[5−7] making them potentially attractive candidates for solar energy conversion.

Most solar cell designs comprise an interface (junction) between two adjoining materials at which the separation of the photogenerated charge carriers occurs. Schottky and p−n junctions have been realized in atomically thin transition metal dichalcogenides (TMDCs) and the capability of 2D crystals for photovoltaics has been demonstrated.[8−11] However, the lateral arrangement of these devices does not allow for easy scalability for which a vertical geometry would be desirable. Such vertical heterostructures can be obtained by stacking of 2D crystals in a layered configuration on top of each other.[12] The van der Waals interaction between adjacent layers keeps the stack together.

These so-called van der Waals heterostructures constitute a new class of designer materials that can be composed of a variety of 2D crystals that are structurally and mechanically similar but exhibit entirely different electronic and optical properties. Hexagonal boron nitride (hBN), for instance, is a wide-gap insulator and optically transparent. It has been employed as electronic barrier in tunneling devices[13,14] and as crystalline substrate.[15,16] Graphene is a semimetal and is typically used as conducting electrode. Another group of 2D crystals are TMDCs, which have the formula MX_2, where M is a transition metal and X = S, Se, or Te. TMDCs exhibit semiconducting behavior[17−20] and have demonstrated considerable potential for acting as active electronic[21−25] and optoelectronic[21,22,26−30] components.

Photodetectors based on graphene/TMDC/graphene stacks[29,30] have shown excellent performance with external quantum efficiency (EQE) of up to 55%. However, such a configuration would not be well suited for photovoltaic energy conversion, because of the low resistance of the unipolar TMDC channel that bypasses the photocurrent source. The generated photovoltage thus varies strongly with illumination intensity and almost vanishes at low light levels, making the total electric power too small for practical applications. By contrast, the photovoltage in a diode configuration is determined by the relative band alignments at the p−n junction and varies only weakly with illumination intensity. In this Letter, we demonstrate that a van der Waals heterojunction made of two different dichalcogenides behaves as a diode and exhibits a photovoltaic effect. The device can thus be employed for solar-energy conversion.

Our devices (see Figure 1a for a schematic drawing) were fabricated on an oxidized silicon (Si) wafer with a 280 nm thick silicon dioxide (SiO_2) layer. They consist of molybdenum

Received: May 26, 2014
Revised: July 15, 2014
Published: July 24, 2014

 © 2014 American Chemical Society dx.doi.org/10.1021/nl501962c | *Nano Lett.* 2014, 14, 4785−4791

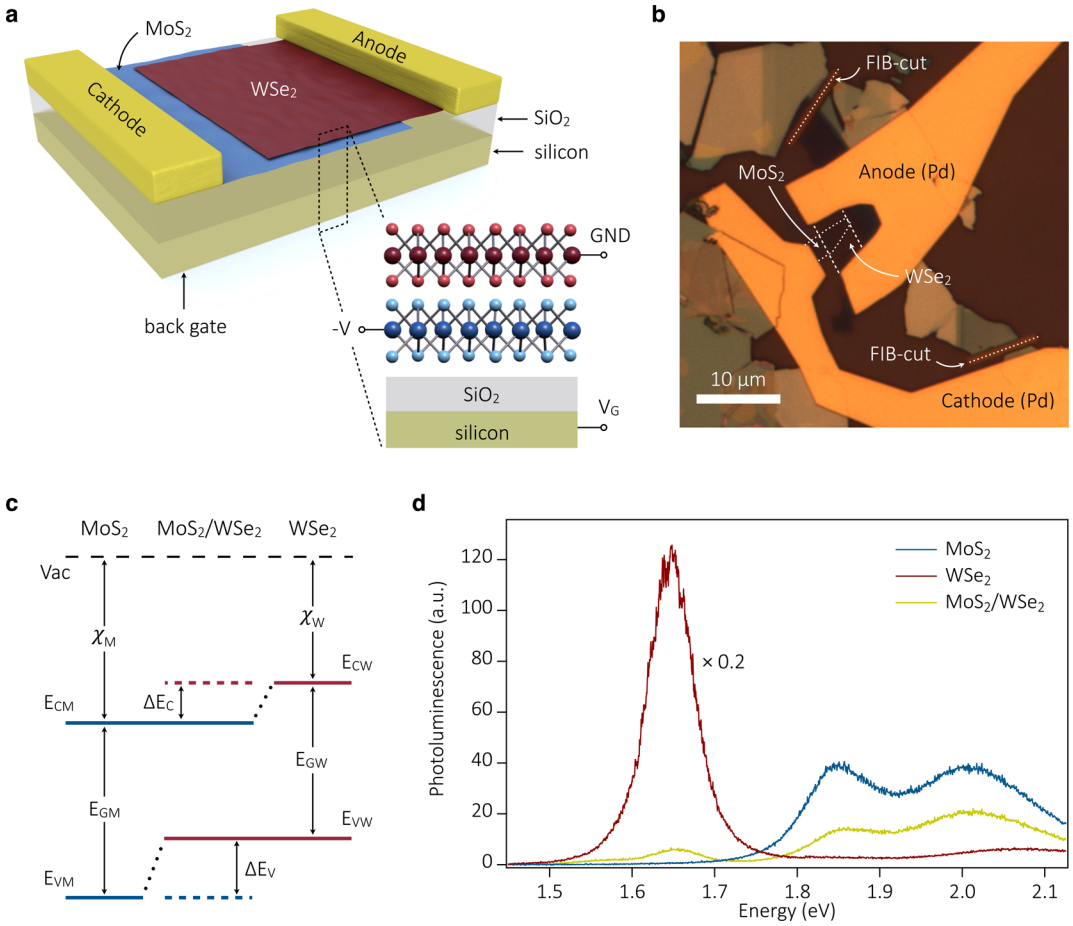

Figure 1. (a) Schematic drawing of the device structure. (b) Microscope image of a typical device. Contact electrodes are made of Pd/Au. The MoS_2 and WSe_2 monolayer flakes are highlighted by dotted and dashed lines, respectively. Short circuits are removed using a focused ion beam (dotted lines). (c) Schematic energy band diagrams of MoS_2 (left; blue lines) and WSe_2 (right; red lines) in the vicinity of the K-point. The MoS_2/WSe_2 heterostructure bands (center) are a superposition of the monolayer bands. The lowest energy electron states (solid blue line) are spatially located in the MoS_2 layer and the highest energy hole states (solid red line) lie in the WSe_2. The excited states are shown as dashed lines. E_C, conduction band edge; E_V, valence band edge; Vac, vacuum level. (d) Photoluminescence measured at different positions on the sample: WSe_2 (red), MoS_2 (blue), MoS_2/WSe_2 heterojunction (yellow). The photoluminescence from the junction is strongly quenched, due to spatial electron−hole separation/exciton dissociation.

disulfide (MoS_2) and tungsten diselenide (WSe_2) monolayers that were mechanically exfoliated from bulk crystals and stacked on top of each other. In a first step, the bottom-layer flake was exfoliated directly onto the Si/SiO_2 substrate, identified by optical microscopy, its thickness verified by Raman (see Supporting Information, Figure S1) and photoluminescence (PL) spectroscopy, and annealed for several hours in vacuum ($\sim 5 \times 10^{-6}$ mbar) at a temperature of $T = 380$ K. In a second step, the top-layer flake was exfoliated onto a stack of polymers on a sacrificial silicon wafer. The polymer stack consisted of poly(acrylic acid) (PAA) and poly(methyl methacrylate) (PMMA) with a thickness chosen such that a monolayer flake could again be identified using a microscope. The PAA was then dissolved in water and the PMMA with the monolayer flake was released from the wafer, turned upside down, and placed with micrometer-precision on top of the other flake with the target wafer kept at $T = 380$ K (above the glass transition temperature of PMMA). Finally, the wafer was cooled down to room temperature and the PMMA was dissolved. Short circuits, caused by chunks of bulk material that are inevitably transferred with the monolayer flake, were removed using a focused ion beam (FIB). After sample fabrication, the devices were annealed again for several hours at $T = 380$ K in vacuum ($\sim 5 \times 10^{-6}$ mbar) to remove resist residues and other contaminants from the sample. A gate voltage V_G, applied to the silicon substrate, controls the electrical characteristics of the heterojunction device. We investigated samples (denoted I, II, and III in the following) with both MoS_2/WSe_2 and WSe_2/MoS_2 layer orders. They all displayed qualitatively similar behavior. Figure 1b shows a microscope image of sample I. A scanning electron microscopy (SEM) image of the device is presented in Supporting Information, Figure S2.

Before we discuss the device operation, let us recall some basic properties of the materials used. Figure 1c shows schematic energy band diagrams of MoS_2 (left) and WSe_2 (right), respectively. Both are direct semiconductors when thinned to monolayer thickness[19,31,32] with conduction band minima and valence band maxima at the K- and K'-points. The absorption spectra of these materials approximately match the solar spectrum, so that they are both suitable as optical absorbers in a photovoltaic cell.[33] In Figure 1d, we show PL spectra obtained by focusing the light from a solid-state laser (532 nm wavelength) onto three different positions on the sample (WSe_2 monolayer, red line; MoS_2 monolayer, blue line;

dx.doi.org/10.1021/nl501962c | Nano Lett. 2014, 14, 4785−4791

MoS_2/WSe_2 heterojunction, yellow line). The individual WSe_2 and MoS_2 monolayers show strong excitonic emission at ~1.65 and ~1.85 eV (A-exciton; ~2.0 eV, B-exciton), respectively, in agreement with previous reports.[19,31,32] Also the higher quantum yield of WSe_2 as compared to MoS_2 has been reported frequently. The suppression of the MoS_2 A-peak with respect to the B-peak indicates strong n-doping of the MoS_2 crystal[34] (see also electrical measurements). The emission from the heterojunction is quenched, as we will discuss below. Given the large exciton binding energies of $E_b \sim 0.5$ eV in WSe_2 and MoS_2 2D materials,[35−37] we estimate electronic band gaps of $E_{GW} \sim 2.15$ eV and $E_{GM} \sim 2.35$ eV. The electron affinity (the energy required to excite an electron from the bottom of the conduction band to vacuum) of MoS_2 is[21] $\chi_M \sim 4.2$ eV. Values reported for monolayer WSe_2 vary but are generally lower[23] ($\chi_W \sim 3.5$−4.0 eV), owing to the smaller electronegativity of W and Se compared to Mo and S.

When brought into contact, an atomically sharp van der Waals heterojunction is formed that is pristine and without broken bonds. The center part of Figure 1c shows the band diagram of the heterojunction, where we assume flat band alignment with the neighboring monolayer regions for simplicity. The exact band lineup will not only be governed by the intrinsic properties of the materials but also by extrinsic factors that vary from sample to sample and are hence difficult to predict. For instance, unintended n-doping is typically observed in natural MoS_2; adsorbed molecules from the ambient will give rise to additional doping. The proposed band diagram can hence only provide a qualitative picture. Because of the large energetic offset of the MoS_2 and WSe_2 states, interlayer coupling is negligible and the heterostructure bands can be considered as a superposition of the monolayer bands.[38] Consequently, the lowest energy electron states are spatially located in the MoS_2 layer and the highest energy hole states lie in the WSe_2, thus forming a type-II heterostructure, as confirmed by band structure calculations[38−40] and recent PL measurements.[41]

In a first step after device fabrication, we acquired the electrical characteristics where the silicon substrate served as a back gate electrode to adjust the doping in the device. Figure 2a shows the current map as a function of gate (V_G) and bias (V) voltages, recorded under biasing conditions as shown in Figure 1a (sample I). The electrical characteristics are different from those obtained in ordinary MoS_2 or WSe_2 field-effect transistors,[17,18,20,23] but can readily be understood by considering an electrical series connection of two such transistors[42] (see also Supporting Information, Figure S3). While the MoS_2-channel remains n-type over most of the observed gate voltage range and gets fully depleted only at $V_G < -71$ V, the WSe_2-channel switches from n-type ($V_G > -11$ V) to p-type ($V_G < -47$ V) due to its ambipolar behavior. In the range -47 V $< V_G < -11$ V the WSe_2-sheet becomes intrinsic and the current flow is suppressed. The less efficient gating of MoS_2 as compared to WSe_2 is mainly attributed to the existence of an impurity band tail underneath the conduction band edge through which the Fermi level moves slowly.[18] The electrical transport in the MoS_2 then occurs by carriers that are thermally activated from impurity states to the conduction band.[43]

The V-dependence of the current is strikingly different in the two on-states. At $V_G > -11$ V, when MoS_2 and WSe_2 are both n-type, current can flow under both V-polarities. In the range -71 V $< V_G < -47$ V, however, the current−voltage (J−V) characteristic exhibits a nonlinear response with current flow

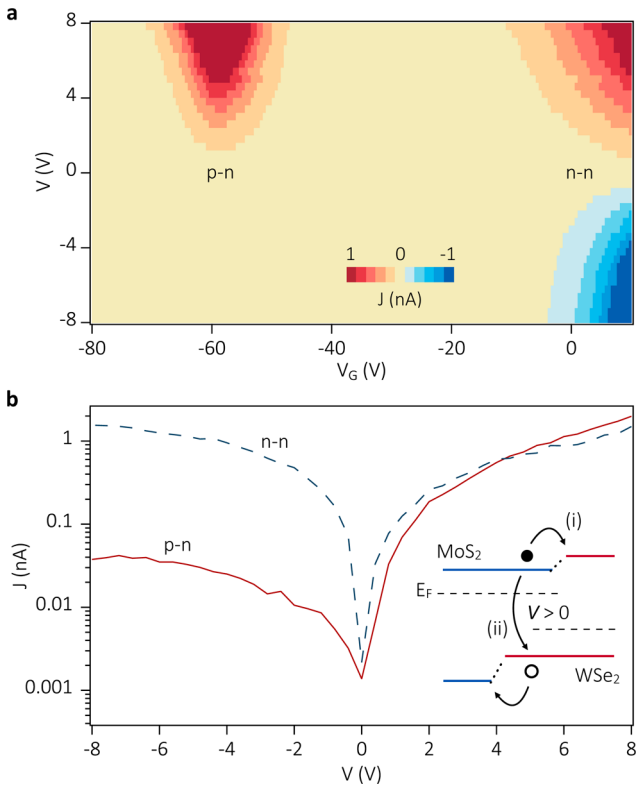

Figure 2. (a) Current map, recorded by scanning gate voltage V_G and bias voltage V. At $V_G > -10$ V, both flakes are n-type and the device shows resistive behavior. In the range -71 V $< V_G < -47$ V, the electrical characteristic exhibits a p−n diode-like behavior. (b) J−V traces obtained under n−n ($V_G = +10$ V; dashed blue line) and p−n ($V_G = -59$ V; solid red line) operation (absolute value of the device current J on a logarithmic scale). Inset: Band diagram under p−n operation and forward bias ($V > 0$). Electrons and holes are injected into the MoS_2 and WSe_2 sheets, respectively, and drift toward the junction where they may (i) overcome the band offsets, or (ii) recombine. E_F, Fermi level.

only under forward ($V > 0$) bias. J−V traces obtained under n−n ($V_G = +10$ V) and p−n ($V_G = -59$ V) configurations are shown in Figure 2b as dashed blue and solid red lines, respectively (the data are also provided on a linear scale in Supporting Information, Figure S4). While the J−V curve of the n−n junction shows symmetric (resistive) behavior, the p−n configuration displays diode-like current rectification, consistent with the type-II band alignment. The forward/reverse current ratio is ~ 50 at $|V| = 8$ V. The electrical characteristics of our device can hence be controlled by electrostatic doping (see also Supporting Information, Figure S5).

Better insight in the diode operation is gained by the band diagram inset in Figure 2b. Forward biasing the diode drives electrons (holes) in MoS_2 (WSe_2) to the heterojunction, where they may either (i) overcome the conduction (valence) band offset ΔE_C (ΔE_V) to be injected into the neighboring layer and drift to the opposite contact electrode, or (ii) recombine so that a continuous current is maintained. At this point, it also becomes clear why we have chosen Pd as a contact metal. Pd has a high-work function which allows for efficient hole injection[44] into WSe_2 but still serves as a reasonably good n-type contact to MoS_2 due to the strong Fermi level pinning in this material.[45]

dx.doi.org/10.1021/nl501962c | Nano Lett. 2014, 14, 4785−4791

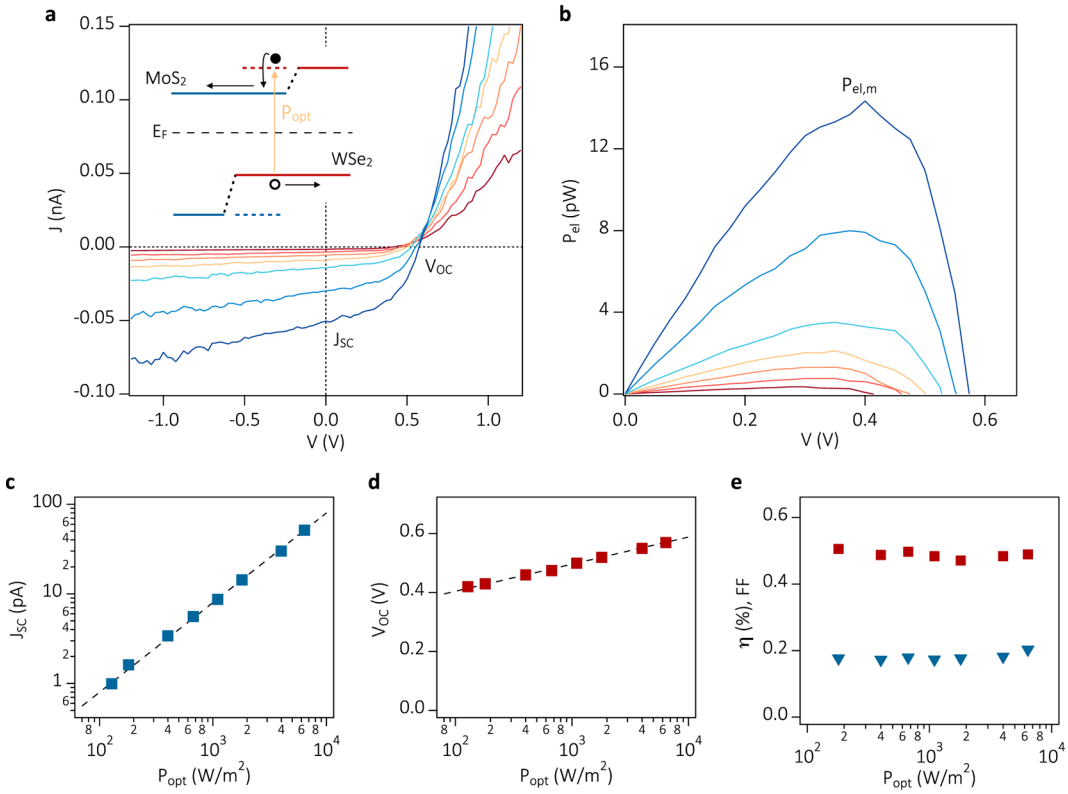

Figure 3. (a) $J-V$ characteristics of the device under optical illumination with P_{opt} = 180, 400, 670, 1100, 1800, 4000, and 6400 W/m^2. (Inset) Schematic illustration of the photovoltaic effect: electron−hole pairs are generated in the heterostructure, relax to the bottom of the conduction and valence bands, and eventually diffuse to the contacts. (b) Electrical power, $P_{el} = J{\cdot}V$, that is extracted from the device. $P_{el,m}$ denotes the output in the maximum power point. (c) Short-circuit current J_{SC} and (d) open-circuit voltage V_{OC}, as extracted from panel a (symbols, experimental data; dashed lines, theoretical fits). (e) Fill factor FF (red rectangles) and power conversion efficiency η (blue triangles). During all measurements the gate bias was fixed at V_G = −50 V.

Figure 3a shows $J-V$ curves upon illumination with white light from a halogen lamp with incident optical power P_{opt} varied between 180 and 6400 W/m^2 (sample II; see electrical characteristics in the dark in Supporting Information, Figure S6). The optical excitation spectrum is provided in Supporting Information, Figure S7. In all measurements, the device is operated in the p−n regime with V_G fixed at −50 V. From the $J-V$ traces it is obvious that the device shows a photovoltaic response, as the curves pass through the fourth quadrant, and electrical power P_{el} can be extracted (Figure 3b). The illumination dependence of the diode series resistance is attributed to photogating of MoS_2. In brief, optically excited carriers are captured in long-lived trap states and increase the MoS_2 conductivity.[26]

Our physical picture of the photoresponse is the following: Photons are absorbed in WSe_2 and MoS_2, resulting in electron−hole pairs (excitons) in both monolayers. Relaxation of the photogenerated carriers then occurs, driven by the type-II band offsets ΔE_C and ΔE_V. As the lowest energy electron and hole states are spatially separated, charge transfer occurs across the heterojunction. The relaxed carriers then diffuse laterally to the contacts, resulting in a photocurrent. Interlayer recombination may occur during diffusion, which reduces the efficiency of the solar cell (in fact, this appears to be the limiting factor for device performance). In the inset of Figure 3a, we schematically illustrate this process for a photon that is absorbed in the WSe_2 layer (an analog diagram can be drawn for photons absorbed in MoS_2; not illustrated, for clarity).

The PL data in Figure 1d support the above interpretation. The luminescence from both layers in the overlap region is quenched (yellow line), indicating strong interlayer coupling. The PL results are inconsistent with type-I band alignment, for which PL quenching for the higher-band gap material (MoS_2) only would be expected. The WSe_2 luminescence is reduced by ∼98%, whereas the reduction in PL from MoS_2 is only ∼65%. This behavior is understood as a result of competition between interlayer charge transfer and (nonradiative) intralayer recombination. The lower luminescence yield of MoS_2 as compared to WSe_2 implies faster intralayer recombination in the former and therefore less efficient charge transfer.

From a molecular perspective, used to describe organic solar cells, our device can be regarded as a heterojunction cell, in which the MoS_2 conduction (E_{CM}) and WSe_2 valence (E_{VW}) bands act as LUMO and HOMO levels, respectively. However, in contrast to organic solar cells, no exciton transport by diffusion is required, because of electron−hole pair generation right at the junction. A spatially resolved photocurrent map (see Supporting Information, Figure S8) was recorded using a tightly focused laser spot (532 nm wavelength) to verify that the photoresponse indeed stems from the laterally extended heterojunction and is not produced at one of the metal−semiconductor contacts.[8]

In Figure 3c,d, we present short-circuit current J_{SC} and open-circuit voltage V_{OC} as a function of illumination intensity (extracted from Figure 3a). J_{SC} scales linearly with P_{opt} and shows no indication of saturation over the measured range of optical powers, which extends to intensities ∼5 times higher

dx.doi.org/10.1021/nl501962c | Nano Lett. 2014, 14, 4785−4791

than the terrestrial solar intensity. We calculate the external quantum efficiency EQE, which is the ratio of the number of collected charge carriers to the number of incident photons, from J_{SC} = EQE × $\lambda q/(hc)$ × P_{opt} ($\lambda \sim 590$ nm is the wavelength, and q, h, and c denote electron charge, Planck's constant, and speed of light, respectively) and obtain EQE ~ 1.5% (dashed line in Figure 3c).

V_{OC} scales with $\ln(P_{opt})$, as expected from conventional p−n junction theory. It is related to the MoS_2 electron and WSe_2 hole carrier densities, n and p, by[46] $qV_{OC} = E_g + k_B T \ln[np/N_c^2]$, where $E_g = |E_{CM} - E_{VW}|$ is the effective band gap, N_c is the effective density of states, and k_B denotes Boltzmann's constant. Under steady-state and open-circuit conditions, the carrier concentrations are determined by the balance between photogeneration ($G \propto P_{opt}$) and interlayer recombination (R) rates. The recombination rate can, in general, be written by the empirical equation[47] $R = \gamma n^\beta$, where γ is a prefactor that is determined by the actual recombination process, β denotes the recombination order, and $n = p$. $\beta = 1$ for monomolecular (Shockley Read Hall; SRH) recombination and $\beta = 2$ for bimolecular (Langevin) recombination. By equating R and G, we obtain the expression

$$\frac{dV_{OC}}{d\ln(P_{opt})} = \frac{2}{\beta}\frac{k_B T}{q}$$

that we fit to the experimental data (dashed line in Figure 3d) and extract $\beta \sim 1.3$. We conclude that the interlayer recombination is dominated by the SRH process, again evidencing the existence of a large density of trap states in TMDCs.

The power conversion efficiency is defined as $\eta = P_{el,m}/P_{opt}$, where $P_{el,m}$ denotes the output at the maximum power point, and is shown in Figure 3e (blue triangles). The fill factor is calculated according to FF = $P_{el,m}/(J_{SC}V_{OC})$ and is plotted in the same figure (red squares). An efficiency of $\eta \sim 0.2\%$ is obtained, which is comparable to values reported for[48] WSe_2 (0.1−0.6%) and[49] MoS_2 (1%) bulk samples, and, more recently, for lateral WSe_2 monolayer p−n junctions[9,10] (0.2−0.5%). The device can also be operated as a photodiode by biasing it in the third quadrant. At $V = -1$ V, a photoresponsivity of $R = J/P_{opt} = 11$ mA/W is achieved. These numbers need to be judged in light of the weak optical absorption of the ultrathin 2D structure. A ~10-fold increase may be achieved by stacking several junctions on top of each other, or by plasmonic enhancement[50] of the optical absorption α. Moreover, given the ~1.5% EQE and assuming α ~10%, we estimate that ~5 times better efficiency could be obtained by sandwiching the dichalcogenide junction between electrodes for vertical carrier extraction.[29,30]

Our spectrally broad white light source not only excites carriers above the electronic band gap, but part of the spectrum also overlaps with below-gap excitons. These can spontaneously dissociate into free (spatially separated) carriers if the respective band offset is greater than the exciton binding energy, ΔE_V (ΔE_C) > E_b. In order to verify whether this condition is fulfilled, we performed J_{SC} measurements under resonant excitation of the WSe_2 ground state exciton at 750 nm wavelength and compared the results with those of above-band gap excitation at 532 nm (see Figure 4a). For a quantitative comparison, we account for the optical interference in the SiO_2 layer by plotting the photocurrent against κP_{opt}, where P_{opt} is the incident power, as usual, and κ accounts for the wavelength-dependent

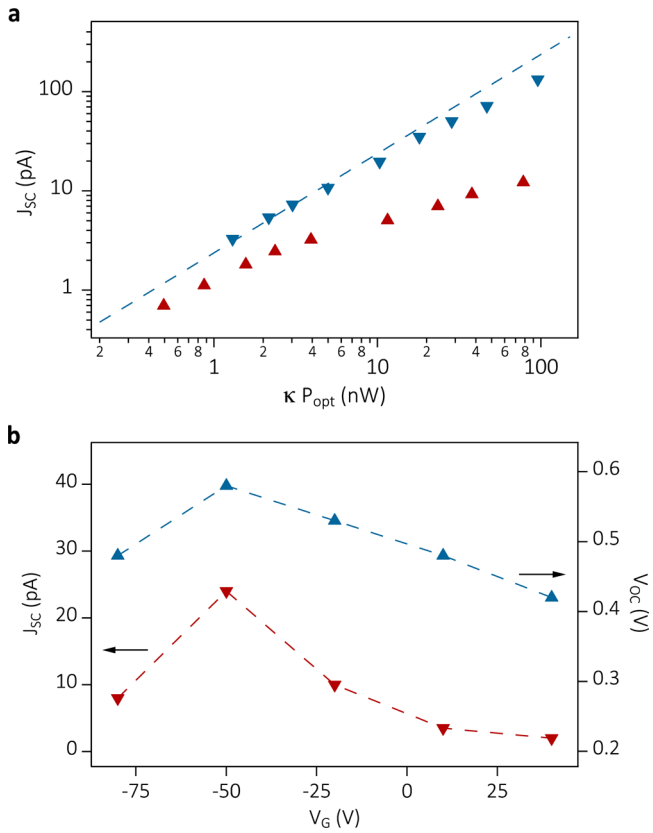

Figure 4. (a) Power dependence of short-circuit current J_{SC} for optical excitation at 532 nm (blue symbols) and 750 nm (red symbols). The optical intensity enhancement κ (see Supporting Information, Figure S9) accounts for standing optical waves in the Si/SiO_2 substrate. The dashed line is a fit of $J_{SC} \propto P_{opt}$. (b) Short-circuit current J_{SC} and the open-circuit voltage V_{OC} are shown as red and blue symbols, respectively (white light illumination, P_{opt} = 3 kW/m^2).

enhancement of the optical intensity (see Supporting Information, Figure S9). As depicted in Figure 4a, the photocurrents are similar at typical solar intensities (~1 kW/m^2 ≃ 1 nW), confirming efficient exciton dissociation. The two processes possess different saturation levels, though. We are currently investigating this behavior in more detail.

In Figure 4b we show J_{SC} (red symbols) and V_{OC} (blue symbols) as a function of gate voltage (see corresponding J−V curves in Supporting Information, Figure S10). The photocurrent peaks in the p−n regime ($V_G = -50$ V), whereas it is suppressed for other gate voltages. The reason for this behavior is two-fold. (i) A large gate-induced excess carrier concentration (electrons in MoS_2 for $V_G \gg -50$ V; holes in WSe_2 for $V_G \ll -50$ V) reduces the carrier lifetime and gives rise to enhanced recombination of the photogenerated carriers. The drop in open-circuit voltage to both sides of the p−n regime provides evidence for this claim. (ii) The carrier collection efficiency depends on V_G because of the gate-dependent band alignment along the channel of the device.

In summary, given the rapid advances in large-scale production of 2D crystals,[5−7] we see potential for using van der Waals heterojunctions in photovoltaic energy conversion. Bringing together different 2D materials in a roll-to-roll process or direct heterostructure growth could lead to a new photovoltaic solar technology. Moreover, due to the plurality of 2D materials with different band gaps and electron affinities, low-cost multijunction solar cells could come within reach.

dx.doi.org/10.1021/nl501962c | Nano Lett. 2014, 14, 4785−4791

Note added: During the finalization of this manuscript we became aware of three related studies.[51−53]

■ ASSOCIATED CONTENT

Supporting Information

Raman spectra, scanning electron microscopy image, further electrical characterization, optical excitation spectrum, photocurrent map, optical absorption enhancement, and gate-dependent $J-V$ characteristics. This material is available free of charge via the Internet at http://pubs.acs.org.

■ AUTHOR INFORMATION

Corresponding Author

*E-mail: thomas.mueller@tuwien.ac.at. Phone: 43-1-58801-38739.

Notes

The authors declare no competing financial interest.

■ ACKNOWLEDGMENTS

We would like to thank G. Kresse, K. Hummer, and K. Unterrainer for valuable discussions, M. Schinnerl, G. D. Cole, and M. Glaser for technical assistance, and E. Bertagnolli and A. Lugstein for providing access to a Raman spectrometer. The research leading to these results has received funding from the Austrian Science Fund FWF (START Y-539) and the European Union Seventh Framework Programme (Grant 604391 Graphene Flagship).

■ REFERENCES

(1) Chapin, D. M.; Fuller, C. S.; Pearson, G. L. *J. Appl. Phys.* **1954**, *25*, 676−677.
(2) Lee, M. M.; Teuscher, J.; Miyasaka, T.; Murakami, T. N.; Snaith, H. J. *Science* **2012**, *338*, 643−647.
(3) Novoselov, K. S.; Geim, A. K.; Morozov, S. V.; Jiang, D.; Zhang, Y.; Dubonos, S. V.; Grigorieva, I. V.; Firsov, A. A. *Science* **2004**, *306*, 666−669.
(4) Novoselov, K. S.; Jiang, D.; Schedin, F.; Booth, T. J.; Khotkevich, V. V.; Morozov, S. V.; Geim, A. K. *Proc. Natl. Acad. Sci. U.S.A.* **2005**, *102*, 10451−10453.
(5) Bae, S.; Kim, H.; Lee, Y.; Xu, X.; Park, J.-S.; Zheng, Y.; Balakrishnan, J.; Lei, T.; Kim, H. R.; Song, Y. I.; Kim, Y.-J.; Kim, K. S.; Özyilmaz, B.; Ahn, J. H.; Hong, B. H.; Iijima, S. *Nat. Nanotechnol.* **2010**, *5*, 574−578.
(6) Liu, K.-K.; Zhang, W.; Lee, Y. H.; Lin, Y. C.; Chang, M. T.; Su, C. Y.; Chang, C. S.; Li, H.; Shi, Y.; Zhang, H.; Lai, C. S.; Li, L. J. *Nano Lett.* **2013**, *12*, 1538−1544.
(7) Huang, J.-K.; Pu, J.; Hsu, C.-L.; Chiu, M.-H.; Juang, Z.-Y.; Chang, Y.-H.; Chang, W.-H.; Iwasa, Y.; Takenobu, T.; Li, L.-J. *ACS Nano* **2014**, *8*, 923−930.
(8) Fontana, M.; Deppe, T.; Boyd, A. K.; Rinzan, M.; Liu, A. Y.; Paranjape, M.; Barbara, P. *Sci. Rep.* **2013**, *3*, 1634.
(9) Pospischil, A.; Furchi, M. M.; Mueller, T. *Nat. Nanotechnol.* **2014**, *9*, 257−261.
(10) Baugher, B. W. H.; Churchill, H. O. H.; Yafang, Y.; Jarillo-Herrero, P. *Nat. Nanotechnol.* **2014**, *9*, 262−267.
(11) Ross, J. S.; Klement, P.; Jones, A. M.; Ghimire, N. J.; Yan, J.; Mandrus, D. G.; Taniguchi, T.; Watanabe, K.; Kitamura, K.; Yao, W.; Cobden, D. H.; Xu, X. *Nat. Nanotechnol.* **2014**, *9*, 268−272.
(12) Geim, A. K.; Grigorieva, I. V. *Nature* **2013**, *499*, 419−425.
(13) Britnell, L.; Gorbachev, R. V.; Jalil, R.; Belle, B. D.; Schedin, F.; Mishchenko, A.; Georgiou, T.; Katsnelson, M. I.; Eaves, L.; Morozov, S. V.; Peres, N. M. R.; Leist, J.; Geim, A. K.; Novoselov, K. S.; Ponomarenko, L. A. *Science* **2013**, *335*, 947−950.
(14) Britnell, L.; Gorbachev, R. V.; Geim, A. K.; Ponomarenko, L. A.; Mishchenko, A.; Greenaway, M. T.; Fromhold, T. M.; Novoselov, K. S.; Eaves, L. *Nat. Commun.* **2013**, *4*, 1794.
(15) Lee, G. H.; Yu, Y.-J.; Cui, X.; Petrone, N.; Lee, C.-H.; Choi, M. S.; Lee, D.-Y.; Lee, C.; Yoo, W. J.; Watanabe, K.; Taniguchi, T.; Nuckolls, C.; Kim, P.; Hone, J. *ACS Nano* **2013**, *7*, 7931−7936.
(16) Dean, C. R.; Young, A. F.; Meric, I.; Lee, C.; Wang, L.; Sorgenfrei, S.; Watanabe, K.; Taniguchi, T.; Kim, P.; Shepard, K. L.; Hone, J. *Nat. Nanotechnol.* **2010**, *5*, 722−726.
(17) Podzorov, V.; Gershenson, M. E.; Kloc, Ch.; Zeis, R.; Bucher, E. *Appl. Phys. Lett.* **2004**, *84*, 3301−3303.
(18) Ayari, A.; Cobas, E.; Ogundadegbe, O.; Fuhrer, M. S. *J. Appl. Phys.* **2007**, *101*, 014507.
(19) Mak, K. F.; Lee, C.; Hone, J.; Shan, J.; Heinz, T. F. *Phys. Rev. Lett.* **2009**, *105*, 115409.
(20) Radisavljevic, B.; Radenovic, A.; Brivio, J.; Giacometti, V.; Kis, A. *Nat. Nanotechnol.* **2011**, *6*, 147−150.
(21) Wang, Q. H.; Kalantar-Zadeh, K.; Kis, A.; Coleman, J. N.; Strano, M. S. *Nat. Nanotechnol.* **2012**, *7*, 699−712.
(22) Jariwala, D.; Sangwan, V. K.; Lauhon, L. J.; Marks, T. J.; Hersam, M. C. *ACS Nano* **2014**, *8*, 1102−1120.
(23) Liu, W.; Kang, J.; Sarkar, D.; Khatami, Y.; Jena, D.; Banerjee, K. *Nano Lett.* **2013**, *13*, 1983−1990.
(24) Georgiou, T.; Jalil, R.; Belle, B. D.; Britnell, L.; Gorbachev, R. V.; Morozov, S. V.; Kim, Y.-J.; Gholinia, A.; Haigh, S. J.; Makarovsky, O.; Eaves, L.; Ponomarenko, L. A.; Geim, A. K.; Novoselov, K. S.; Mishchenko, A. *Nat. Nanotechnol.* **2013**, *8*, 100−103.
(25) Wang, H.; Yu, L.; Lee, Y.-H.; Shi, Y.; Hsu, A.; Chin, M. L.; Li, L.-J.; Dubey, M.; Kong, J.; Palacios, T. *Nano Lett.* **2012**, *12*, 4674−4680.
(26) Lopez-Sanchez, O.; Lembke, D.; Kayci, M.; Radenovic, A.; Kis, A. *Nat. Nanotechnol.* **2013**, *8*, 497−501.
(27) Roy, K.; Padmanabhan, M.; Goswami, S.; Sai, T. P.; Ramalingam, G.; Raghavan, S.; Ghosh, A. *Nat. Nanotechnol.* **2013**, *8*, 826−830.
(28) Zhang, W.; Chuu, C.-P.; Huang, J.-K.; Chen, C.-H.; Tsai, M.-L.; Chang, Y.-H.; Liang, C.-T.; Chen, Y.-Z.; Chueh, Y.-L.; He, J.-H.; Chou, M.-Y.; Li, L.-J. *Sci. Rep.* **2013**, *4*, 3826.
(29) Britnell, L.; Ribeiro, R. M.; Eckmann, A.; Jalil, R.; Belle, B. D.; Mishchenko, A.; Kim, Y.-J.; Gorbachev, R. V.; Georgiou, T.; Morozov, S. V.; Grigorenko, A. N.; Geim, A. K.; Casiraghi, C.; Castro Neto, A. H.; Novoselov, K. S. *Science* **2013**, *340*, 1311−1314.
(30) Yu, W. J.; Liu, Y.; Zhou, H.; Yin, A.; Li, Z.; Huang, Y.; Duan, X. *Nat. Nanotechnol.* **2013**, *8*, 952−958.
(31) Splendiani, A.; Sun, L.; Zhang, Y.; Li, T.; Kim, J.; Chim, C.-Y.; Galli, G.; Wang, F. *Nano Lett.* **2010**, *10*, 1271−1275.
(32) Tonndorf, P.; Schmidt, R.; Böttger, P.; Zhang, X.; Börner, J.; Liebig, A.; Albrecht, M.; Kloc, C.; Gordan, O.; Zahn, D. R. T.; de Vasconcellos, S. M.; Bratschitsch, R. *Opt. Express* **2013**, *21*, 4908−4916.
(33) Bernardi, M.; Palummo, M.; Grossman, J. C. *Nano Lett.* **2013**, *13*, 3664−3670.
(34) Mouri, S.; Miyauchi, Y.; Matsuda, K. *Nano Lett.* **2013**, *13*, 5944−5948.
(35) Berkelbach, T. C.; Hybertsen, M. S.; Reichman, D. R. *Phys. Rev. B* **2013**, *88*, 045318.
(36) Klots, A. R.; Newaz, A. K. M.; Wang, B.; Prasai, D.; Krzyzanowska, H.; Caudel, D.; Ghimire, N. J.; Yan, J.; Ivanov, B. L.; Velizhanin, K. A.; Burger, A.; Mandrus, D. G.; Tolk, N. H.; Pantelides, S. T.; Bolotin, K. I. arXiv:1403.6455 2014 (accessed Mar 25, 2014).
(37) Wang, G.; Marie, X.; Gerber, I.; Amand, T.; Lagarde, D.; Bouet, L.; Vidal, M.; Balocchi, A.; Urbaszek, B. arXiv:1404.0056 2014 (accessed Mar 31, 2014).
(38) Kośmider, K.; Fernández-Rossier, J. *Phys. Rev. B* **2013**, *87*, 075451.
(39) Kang, J.; Tongay, S.; Zhou, J.; Li, J.; Wu, J. *Appl. Phys. Lett.* **2013**, *102*, 012111.
(40) Komsa, H.-P.; Krasheninnikov, A. V. *Phys. Rev. B* **2013**, *88*, 085318.
(41) Rivera, P.; Schaibley, J. R.; Jones, A. M.; Ross, J. S.; Wu, S.; Aivazian, G.; Klement, P.; Ghimire, N. J.; Yan, J.; Mandrus, D. G.; Yao, W.; Xu, X. arXiv:1403.4985 2014 (accessed Mar 19, 2014).

(42) Jariwala, D.; Sangwan, V. K.; Wu, C.-C.; Prabhumirashi, P. L.; Geier, M. L.; Marks, T. J.; Lauhon, L. J.; Hersam, M. C. *Proc. Natl. Acad. Sci. U.S.A.* **2013**, *110*, 18076−18080.
(43) Ghatak, S.; Pal, A. N.; Ghosh, A. *ACS Nano* **2011**, *5*, 7707−7712.
(44) Fang, H.; Chuang, S.; Chang, T. C.; Takei, K.; Takahashi, T.; Javey, A. *Nano Lett.* **2012**, *12*, 3788−3792.
(45) Das, S.; Chen, H.-Y.; Penumatcha, A. V.; Appenzeller, J. *Nano Lett.* **2013**, *13*, 100−105.
(46) Cheyns, D.; Poortmans, J.; Heremans, P.; Deibel, C.; Verlaak, S.; Rand, B. P.; Genoe, J. *Phys. Rev. B* **2008**, *77*, 165332.
(47) Rauh, D.; Deibel, C.; Dyakonov, V. *Adv. Funct. Mater.* **2012**, *22*, 3371−3377.
(48) Späh, R.; Elrod, U.; LuxSteiner, M.; Bucher, E.; Wagner, S. *Appl. Phys. Lett.* **1983**, *43*, 79−81.
(49) Fortin, E.; Sears, W. M. *J. Phys. Chem. Solids* **1982**, *43*, 881−884.
(50) Echtermeyer, T. J.; Britnell, L.; Jasnos, P. K.; Lombardo, A.; Gorbachev, R. V.; Grigorenko, A. N.; Geim, A. K.; Ferrari, A. C.; Novoselov, K. S. *Nat. Commun.* **2011**, *2*, 458.
(51) Lee, C.-H.; Lee, G.-H.; van der Zande, A. M.; Chen, W.; Li, Y.; Han, M.; Cui, X.; Arefe, G.; Nuckolls, C.; Heinz, T. F.; Guo, J.; Hone, J.; Kim, P. arXiv:1403.3062 2014 (accessed Mar 12, 2014).
(52) Cheng, R.; Li, D.; Zhou, H.; Wang, C.; Yin, A.; Jiang, S.; Liu, Y.; Chen, Y.; Huang, Y.; Duan, X. arXiv:1403.3447 2014 (accessed Mar 13, 2014).
(53) Fang, H.; Battaglia, C.; Carraro, C.; Nemsak, S.; Ozdol, B.; Kang, J. S.; Bechtel, H. A.; Desai, S. B.; Kronast, F.; Unal, A. A.; Conti, G.; Conlon, C.; Palsson, G. K.; Martin, M. C.; Minor, A. M.; Fadley, C. S.; Yablonovitch, E.; Maboudian, R.; Javey, A. *Proc. Natl. Acad. Sci. U.S.A.* **2014**, *111*, 6198−6202.